Chapter 4

A Double Heterojunction n-i-p Photodetector Based on Mercury Cadmium Telluride for Terahertz Applications

4.1 Introduction

Research in the THz region has drawn considerable attention because of its potential to serve applications requiring high bandwidth with relatively high security to eavesdropping. The advances in the material research have made it possible to achieve the breakthrough applications in the THz region. Numerous applications previously considered as speculative like medical diagnosis, security screening, bomb detection, THz wireless communications etc., becoming more realistic [119]-[120], [130]. All these factors have contributed for taking the research direction in the THz field to the next level and the devices thus developed accessible to all. Besides, many companies' interest, investment, and participation in this research field started yielding good results. HgCdTe, because of its unique properties is chosen for the development of photodetectors for THz applications. As discussed in the previous chapter, there is a scope for further reduction in the dark current and enhancement in the optical characteristics of the device. To achieve it, a modification has been made to the structure used in chapter 1. We have introduced a one more heterojunction in the n-i-p photodetector, thus the device now contains two heterojunctions. A very few works are carried out using HgCdTe material for the detection of the THz radiation [117]-[118]. Usually, the photodetectors based on MCT are grown on the very expensive lattice matched CdZnTe substrates. Precise growth is another issue associated with CdZnTe. Other low-cost alternate substrates like GaAs can also be used. But the problem associated with it is the lattice mismatch with the MCT [131]. In the proposed structure, the effect of substrate is not considered since the front illumination technique is used [115]-[116], [121]-[123], [132]-[133]. In this chapter, a $N^{+} - CdTe/\, n^{0} -$

$Hg_{0.824675}Cd_{0.175325}Te\ /P^{+} - Hg_{0.778299}Cd_{0.221701}Te$ n-i-p double hetero-junction photodetector is proposed at an operating wavelength of 30 µm. As discussed earlier, narrow bandgap semiconductors suffer from large leakage currents at room temperature. Hence, they require cryogenic cooling to avoid it. The thermal effects in the devices are reduced by lower temperatures. Therefore, the device has been operated at 77 K. Since the device is operated at cryogenic cooling temperature, it is not portable and very costly. For numerical simulation, ATLAS™ TCAD tool is used. Analytical simulation is carried out in MATLAB by applying appropriate boundary conditions and solving closed-form equations. For obtaining electrical characteristics, the device is simulated with aspects like the electric field, energy band diagram, and dark current. Similarly, for optical characteristics, the device is simulated in terms of spectral response, quantum efficiency, responsivity and detectivity. For the above, closed-form equations for diffusion current under dark and illuminated conditions and quantum efficiency equations have been derived by solving diffusion equations employing proper boundary conditions. The results obtained from the double hetero-junction shows enhancement in the optoelectronic properties in comparison to the work reported in chapter 3 [134] of single heterojunction photodetector.

4.2 Device structure and material parameters

The proposed device primarily consists of three layers. The top layer (N^{+}- region) is made of a wide bandgap material CdTe that has minimal lattice mismatch with the $Hg_{1-x}Cd_{x}Te$ [124]. It serves the purpose of a transparent/window layer. The second region i.e., active region is made of $Hg_{1-x}Cd_{x}Te$ with x-composition ($x = 0.175325$) selected to absorb the incoming radiation of a wavelength of 30 µm. Its width is chosen wide enough to have good absorption of the incident THz radiation. The window layer and the active layer forms one heterojunction.

The third region (P^+ region) is made of $Hg_{1-y}Cd_yTe$ that has composition ($y = 0.221701$) different from the active layer. It also forms a heterojunction with the active layer. Therefore, the photodetector proposed comprises of two heterojunctions. The parameters d_n, d_p, t are the thicknesses of $N^+ - CdTe$ layer, $P^+ - Hg_{1-x}Cd_xTe$ layer and $n^0 - Hg_{1-x}Cd_xTe$ layer respectively. The quantities x_n and x_p are the depletion region widths in the active layer and P^+ regions respectively. The entire structure is grown epitaxially on a lattice-matched CdZnTe substrate. Both the cladding layers are doped to $10^{24}\ m^{-3}$ and the active layer is lightly doped to $10^{21}\ m^{-3}$. As the material chosen for absorption is a narrow bandgap material, they need to be cooled down to suppress the dark current. Therefore, the device has been operated at 77 K. The light is incident on the top layer i.e., CdTe.

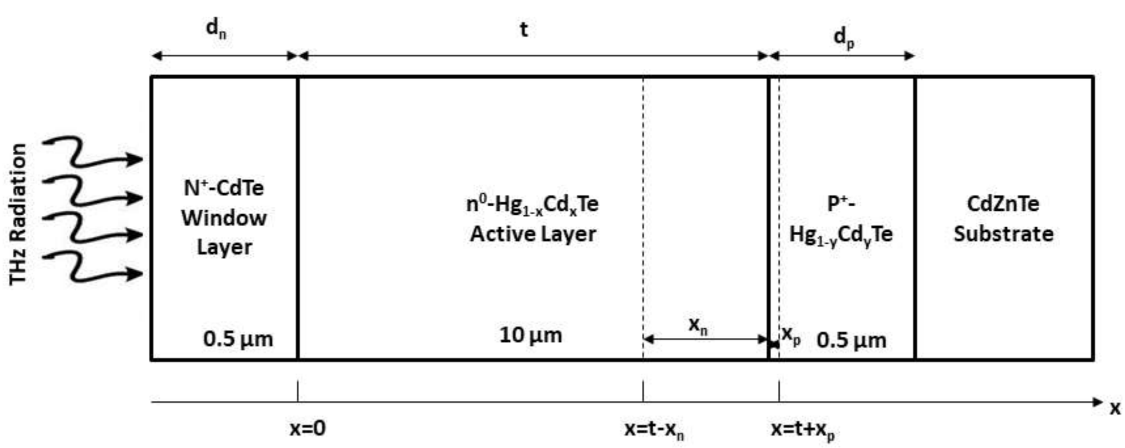

Fig.4.1 Proposed N^+-i-P^+ double heterojunction photodetector

The incident photons with energy lower than the bandgap of the CdTe material crosses the N^+ region with negligible absorption and gets absorbed mostly in the narrow bandgap $Hg_{1-x}Cd_xTe$ (active region) creating electron-hole pairs. The two heterojunctions accounts for the reduction of the dark current as barriers are formed on both sides of the active region preventing diffusion of carriers. In addition, the presence of two heterojunctions aids in better carrier confinement in the active layer due to the discontinuities in the band structure [132]. Under reverse bias, the strong electric fields developed at the two hetero interfaces accounts for the sweeping of the photo-generated carriers reaching the electrodes. Thus, resulting in enhanced optical characteristics.

Table 4.1 Parameters used for Device Analysis at 77 K.

Sl. No.	Parameters	$N^+ - CdTe$	$n^0 - Hg_{1-x}Cd_xTe$	$P^+ - Hg_{1-y}Cd_yTe$
1	Composition	-	0.175325	0.221701
2	Bandgap (meV)	1608.8	41.4	117.0
3	Electron Affinity (eV)	2.9880	4.2639	4.2023
4	Relative Permittivity	10.6000	17.9414	17.3216
5	$N_C(m^{-3})$	1.1394×10^{23}	5.9242×10^{20}	2.7415×10^{21}
6	$N_V(m^{-3})$	1.7485×10^{24}	1.3301×10^{24}	1.5166×10^{24}
7	$n_i(m^{-3})$	-	1.2485×10^{21}	8.6378×10^{18}
8	Doping (m^{-3})	10^{24}	10^{21}	10^{24}

The parameters given in Table 4.1 except doping have been calculated following the empirical formulae as given in reference [107] and have been included in the device analysis in the ATLAS simulation code for optoelectronic characteristics.

4.3 Simulation Methodology

As discussed in the previous chapter, numerical simulation is carried out in the ATLAS™ device simulator that employs a Finite Element Method (FEM) to obtain the optoelectronic characteristics of the semiconductor device. The simulator predicts the electrical behaviour as well as optical behaviour and helps in the design of high-performance devices. It provides the solution to a set of equations that include Poisson's equation, continuity equations and transport equations which were discussed in the previous chapter [134]. LUMINOUS, an integral part of ATLAS tool helps in finding out the photogeneration at each mesh point of the structure. The optical characteristics are not computed directly by LUMIOUS. It uses the ray tracing method to determine the optical intensity at each mesh point by taking the refractive index and the extinction coefficient of the materials considered. It computes only the currents generated and uses them for determination of the optical characteristics like quantum efficiency, and responsivity. LUMINOUS employs two equations for the computation of the optical characteristics. It is necessary to know how much current the source beam generates and the available photocurrent once it is incident on the device.

The simulation employs a source of light which is monochromatic in nature and is given as [134]

$$I_s = q\frac{B_n\lambda}{hc}W_t \tag{4.1}$$

Usually, this equation 4.1 can be used for n number of beams with different beam intensities. Since monochromatic source is used, therefore B_n represents only the beam intensity of the monochromatic source.

Once the monochromatic light source is incident on the device, depending on the material properties, the available photocurrent can be computed as given [116]

$$I_A = q\frac{B_n\lambda}{hc}\sum_{i=1}^{N_R} W_R\int_0^{Y_i} P_i\alpha_i e^{-\alpha_i y}dy \tag{4.2}$$

4.4 Analytical Modeling

4.4.1 Dark Current Modeling

The computation of dark current involves solving of the diffusion currents, the generation recombination currents and the tunneling currents [134]-[136]. In the photodetector designed, the diffusion currents are derived and computed following the boundary conditions of the device [134]. For better and accurate modeling, the diffusion of carriers from P^+ to n^0 region and the diffusion of carriers from n^0 to P^+ region respectively have been considered and are expressed as shown below.

$$(I_p)_n = \frac{qn_i^2 A}{N_D}\frac{D_p}{L_p}\left\{\frac{\frac{S_p L_p}{D_p}cosh\left(\frac{t-x_n}{L_p}\right)-sinh\left(\frac{t-x_n}{L_p}\right)}{cosh\left(\frac{t-x_n}{L_p}\right)-\frac{S_p L_p}{D_p}sinh\left(\frac{t-x_n}{L_p}\right)}\right\}\left(exp\left(\frac{-q(V_d-\Delta E_v)}{kT}\right)\right) \quad (4.3)$$

$$(I_n)_p = \frac{qn_i^2 A}{N_A}\frac{D_n}{L_n}\left\{\frac{\frac{S_n L_n}{D_n}cosh\left(\frac{d_p-x_p}{L_n}\right)-sinh\left(\frac{d_p-x_p}{L_n}\right)}{cosh\left(\frac{d_p-x_p}{L_n}\right)-\frac{S_n L_n}{D_n}sinh\left(\frac{d_p-x_p}{L_n}\right)}\right\}\left(exp\left(\frac{-q(V_d-\Delta E_c)}{kT}\right)\right) \quad (4.4)$$

where ΔE_c and ΔE_v represent the conduction band and valence band offsets.

The diffusion current is the combination of equations (4.3) and (4.4) and is expressed as

$$I_{DIFF} = \left((I_p)_n + (I_n)_p\right)\left(exp\left(\frac{qV}{kT}\right)-1\right) \quad (4.5)$$

The other currents like generation-recombination currents, tunneling currents have been modeled in determining the dark current [129].

The total dark current is the sum of contributions from diffusion current, generation recombination currents and tunneling currents.

$$I_{DARK} = I_{DIFF} + I_{GR} + I_{Tun} \tag{4.6}$$

4.4.2 Optical Characterization

It is necessary to solve the continuity equations through proper boundary conditions to determine the quantum efficiency of the photodetector device considered. It has been computed considering three regions of the photodetector i.e., two neutral regions and the depletion region. Quantum efficiency equations have been taken from the reference [129], [133]. Once the quantum efficiency of the device is computed for different wavelengths, the other optical characteristics can be determined.

One of the important figures of merit of a photodetector is the specific detectivity D^*. It is expressed as given below

$$Specific\ Detectivity(D^*) = \frac{q\eta\lambda}{hc}\sqrt{\frac{(RA)_{NET}}{kT}} \tag{4.7}$$

The $(RA)_{NET}$ is the contribution of resistance area products from the diffusion, generation recombination and tunneling currents.

Another important figure of merit of a photodetector is the current responsivity $(\Re)$ and is expressed as

$$Responsivity(\Re) = \frac{q\eta\lambda}{hc} \tag{4.8}$$

The noise equivalent power (NEP) of a photodetector is a measure of sensitivity of the device. NEP should be as low as possible to detect the weak signals and is expressed as

$$NEP = \frac{\sqrt{A\,B}}{D^*} \tag{4.9}$$

4.5 Results and Discussion

The proposed photodetector structure consists of two heterojunctions. Numerical simulations were carried out in the ATLAS™ TCAD tool and subsequently verified the results analytically through MATLAB simulation. The electric and the optical characteristics are simulated utilizing BLAZE and LUMINOUS tools that are interfaced with the ATLAS™. BLAZE is basically used for II-VI compound materials and heterojunctions. The dimensions of the device, doping concentrations are kept the same as discussed in the previous chapter [134]. The only change is that the third region which was forming a homojunction with the active region previously, is now chosen to have a composition such that it forms a heterojunction with the active region. The values of N_C, N_V are computed for all the three regions. Also, the effective lifetime of the carriers has been computed taking into consideration all the recombination mechanisms and is included in the DECKBUILD code as a part of material model specification. In the active layer i.e., $Hg_{1-x}Cd_xTe$, the cadmium mole fraction of the material is computed to have the bandgap of the material that corresponds to the cut-off wavelength of 30 μm. In determining the optical characteristics, the absorption coefficients of the materials of the three regions of the photodetector are calculated by employing Chu's absorption methods [113], [127]. Computation of absorption coefficients helps in finding out the refractive index and extinction coefficient of the materials with respect to the wavelength. In the numerical simulation, the inclusion of the (n, k) data file in the DECKBUILD code provides the optical characteristics of the photodetector. A front illumination technique has been employed in the device under consideration. The CdTe which is a wide bandgap material is almost transparent to the incoming radiation. Mostly the absorption takes place in the active layer. The double heterojunction in the photodetector form barriers on either side of the active layer preventing the diffusion of carriers and thus reduction in dark current. Also, greater carrier confinement is possible in the active region. Strong electric fields will be developed at the two hetero interfaces and therefore results in enhanced optical characteristics.

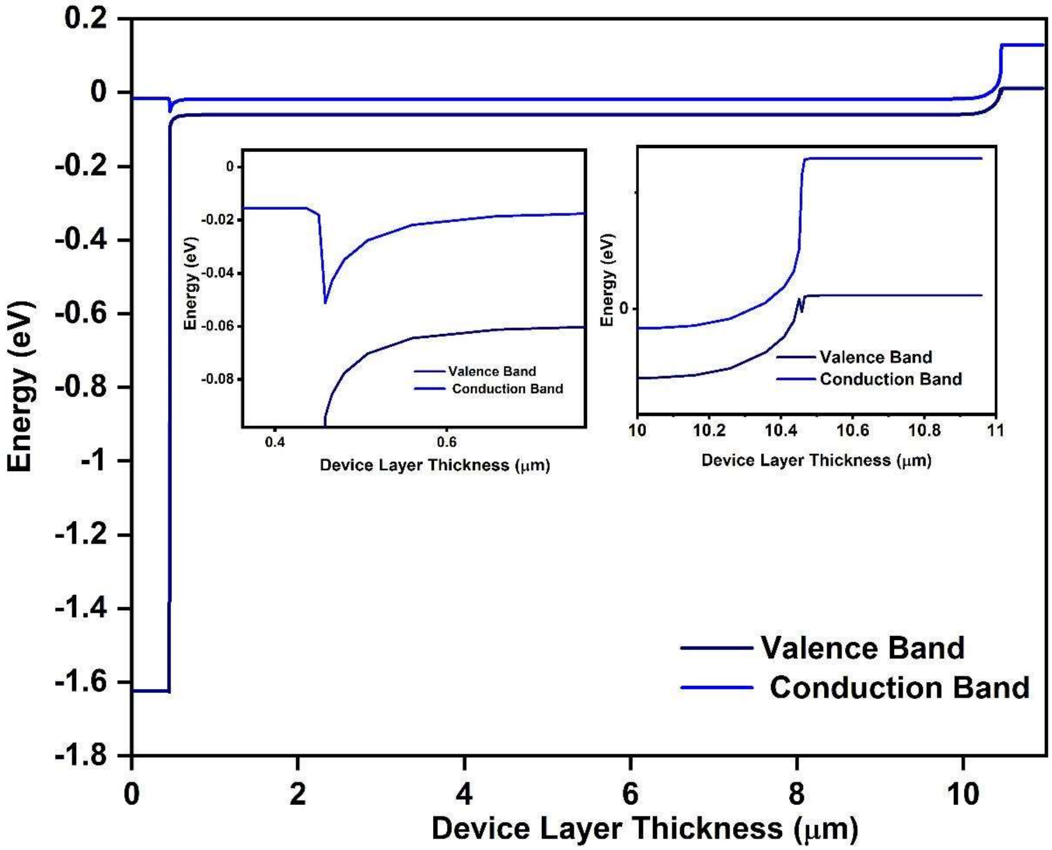

Fig.4.2 Energy band diagram of the double heterojunction photodetector in equilibrium condition

The formation of heterojunctions can be observed at the interfaces of $N^{+} - CdTe/n^{0} - Hg_{0.824675}Cd_{0.175325}Te$ and $n^{0} - Hg_{0.824675}Cd_{0.175325}Te\ /P^{+} - Hg_{0.778299}Cd_{0.221701}Te$ in Fig.4.2 which were clearly shown in the inset.

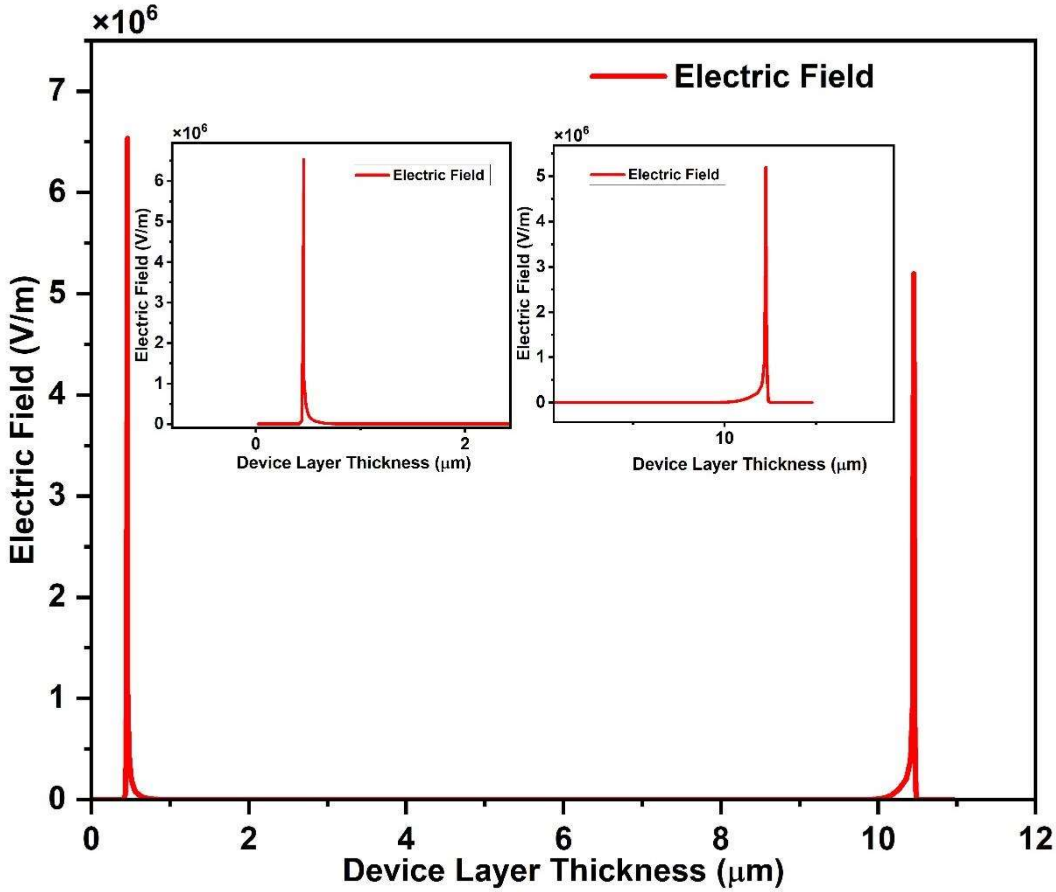

Fig.4.3 Electric field profile of the double heterojunction photodetector in an unbiased condition

In Fig.4.3, it can be observed that there are two peaks at the two hetero interfaces indicating the strong electric fields developed. The device is found to exhibit an electric field of $6.53\ X\ 10^6\ V/m$ at the $N^+ - CdTe$ / $n^0 - Hg_{0.824675}Cd_{0.175325}Te$ hetero interface and $5.19\ X\ 10^6\ V/m$ at the $n^0 - Hg_{0.824675}Cd_{0.175325}Te$ / $P^+ - Hg_{0.778299}Cd_{0.221701}Te$ hetero interface.

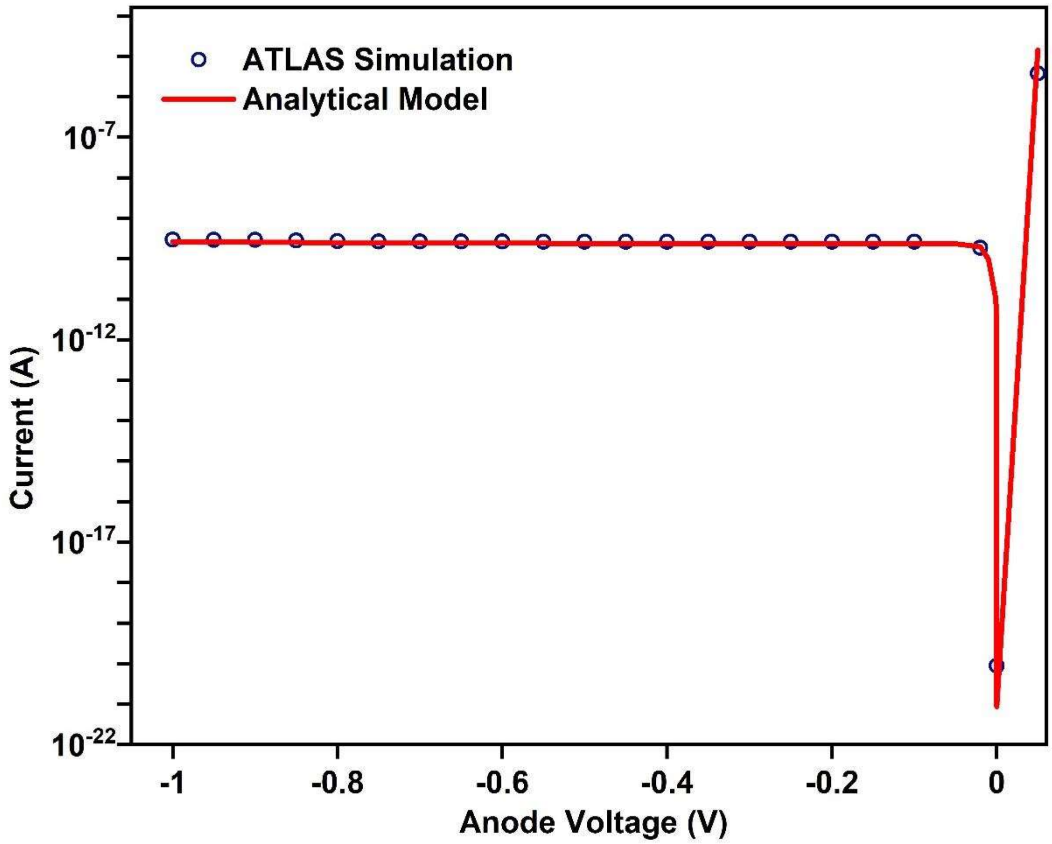

Fig.4.4 Dark current versus applied voltage bias

Fig.4.4 shows the variation of the dark current in accordance with the applied voltage. The addition of second heterojunction accounted for greater reduction in dark current. The results obtained from numerical simulation and analytical modeling are compared. They are found to be matching. The device is operated at a reverse bias of 0.5 V and it exhibited a dark current of $2.42 \times 10^{-10} A$.

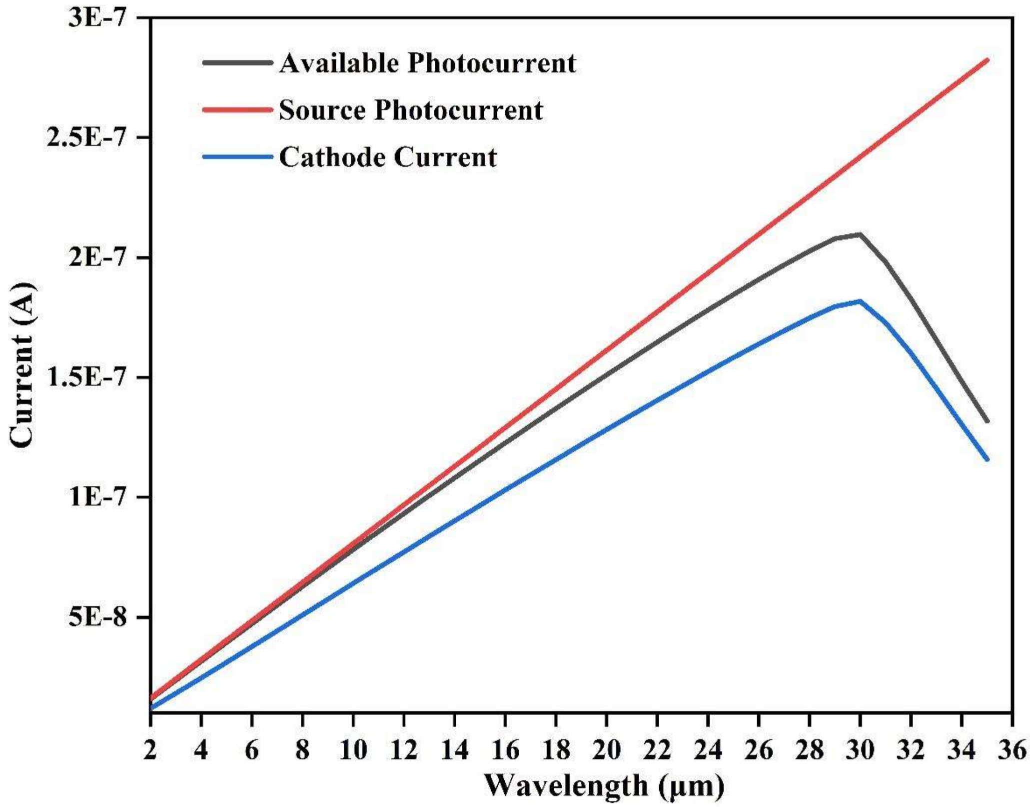

Fig.4.5 Spectral Response of the double heterojunction photodetector

Fig.4.5 shows the spectral response of the photodetector. It can be seen from the figure that the cathode current i.e., the photocurrent under illumination condition increases with the wavelength of operation. Its value will be maximum at a cut-off wavelength of 30 μm. Beyond it, there is a fall in the current for longer wavelengths owing to the strong recombination of carriers.

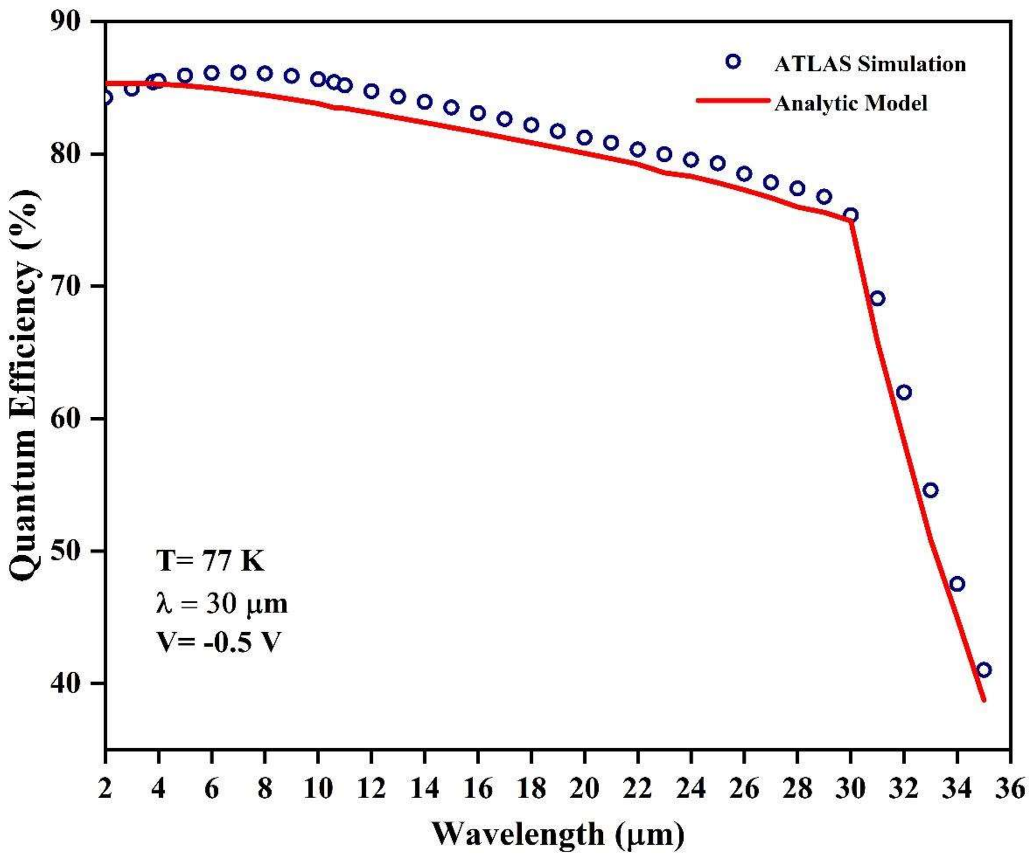

Fig.4.6 Variation of quantum efficiency versus wavelength at a reverse bias of V=0.5 V

The presence of second heterojunction accounted for greater carrier confinement in the active layer, therefore increased quantum efficiency. The device is found to exhibit a quantum efficiency of 75.35 %. As seen in Fig.4.6, the results obtained from ATLAS and analytical model are in close agreement.

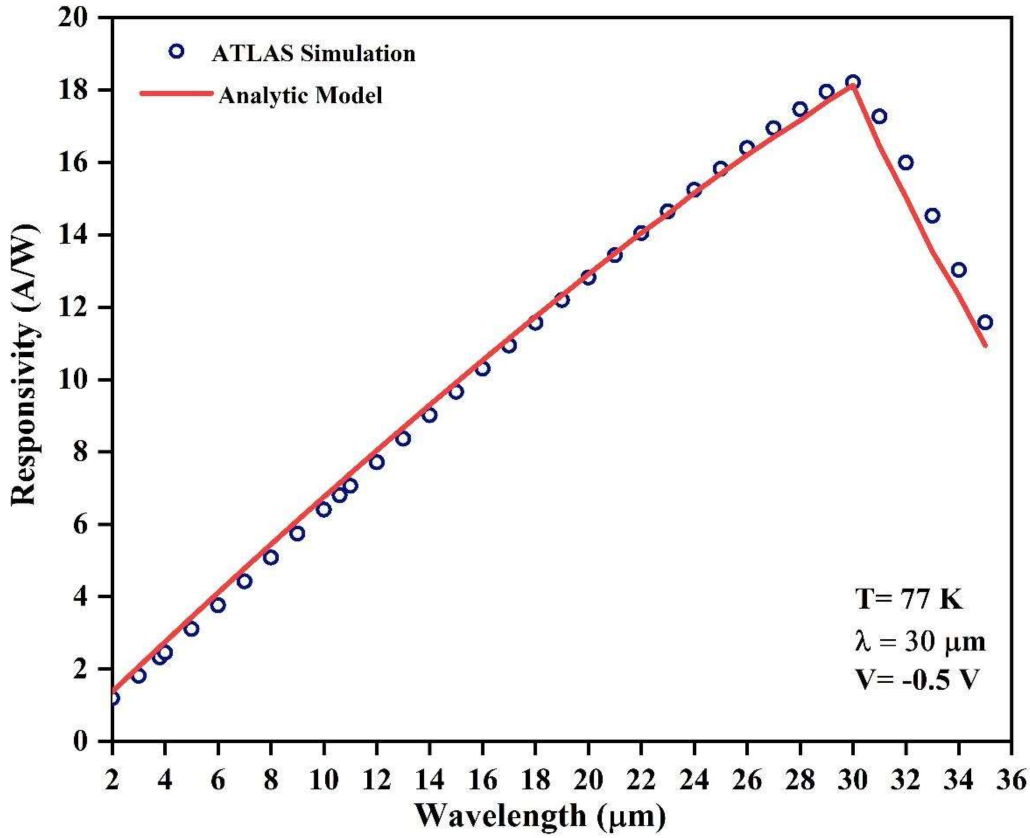

Fig.4.7 Variation of responsivity versus wavelength at a reverse bias of V=0.5 V

In the Fig.4.7, a peak responsivity of ~18.21 A/W is observed at the cut-off wavelength of 30 μm. A fall is observed beyond the cut-off wavelength, as the carrier generation in the active region reduces due to a decrease in the absorption rate. We can observe that the results obtained on the basis on ATLAS simulation are in close agreement with results obtained from the analytical modeling.

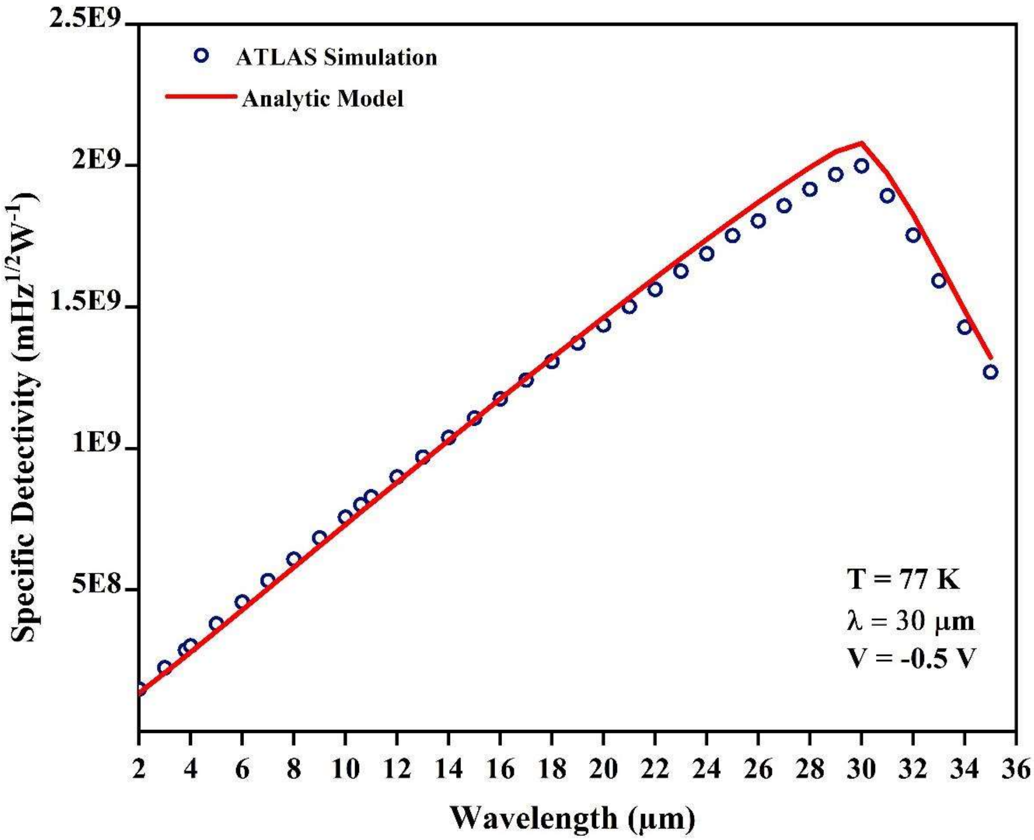

Fig.4.8 Variation of specific detectivity versus wavelength at a reverse bias of V=0.5 V

It can be observed that the dark current of the double heterojunction proposed is less than the single heterojunction discussed in the previous chapter. As the specific detectivity depends on the dark current, the proposed device has an improvement in the value of specific detectivity in comparison to single heterojunction device in the previous chapter. The device exhibited a peak specific detectivity of $1.99 \times 10^9\ mHz^{1/2}$ at the cut-off wavelength of 30 μm and beyond it, for longer wavelengths, there is a fall in the specific detectivity. The results obtained on the basis of analytical model closely matches with the results of ATLAS simulation.

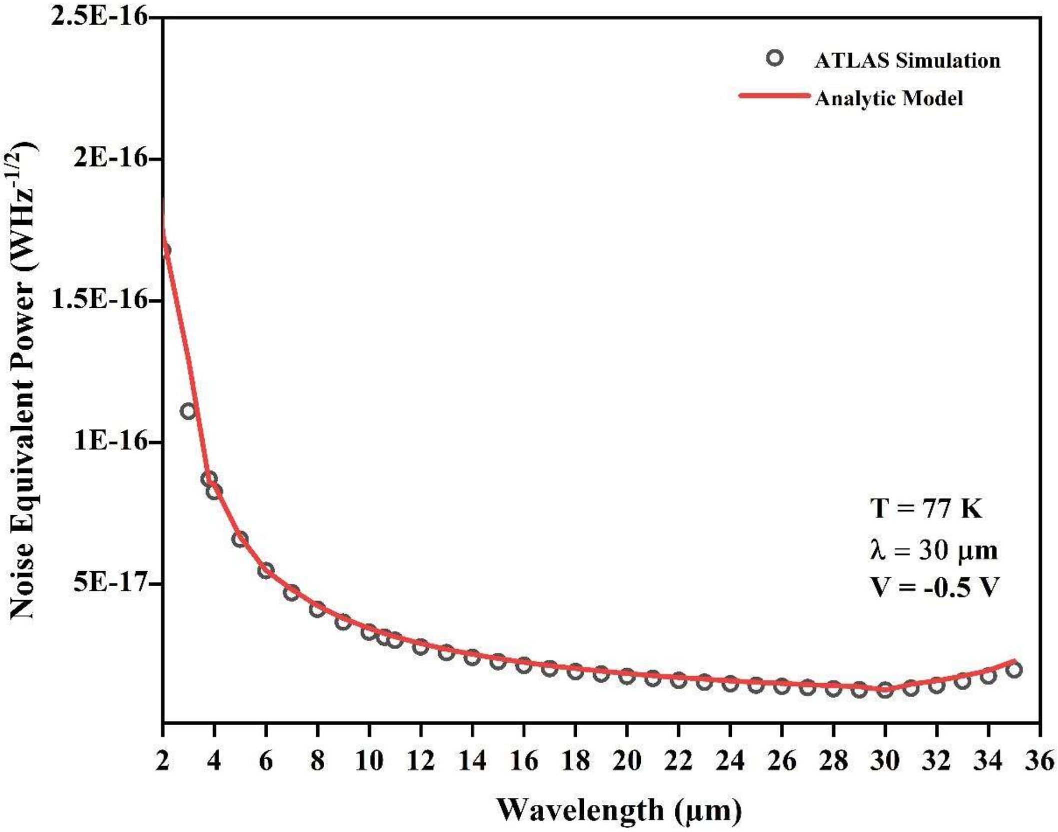

Fig.4.9 Variation of noise equivalent power (NEP) versus wavelength at a reverse bias of V=0.5 V

As NEP is inversely proportional to the specific detectivity, it can be seen in the Fig.4.9 that the photodetector exhibits a very low NEP value of ~$0.21 \times 10^{-16} \frac{W}{\sqrt{Hz}}$ at a wavelength of 30 µm. So, it can be concluded that the photodetector proposed detects even the weakest of signals in comparison to the single heterojunction photodetector. All the results obtained through numerical simulation are in a close match with results obtained from the analytical modeling.

Table 4.2 Comparison of single and double heterojunction photodetectors optoelectronic characteristics for a -0.5 V bias at a temperature of 77 K under 10^4 W/m^2 incident optical power density at a 30 µm operating wavelength

Sl. No.	Parameters	Single Hetero-junction photodetector [134]	Double Hetero-Junction photodetector (Proposed)
1	I_{dark} (A)	4.6 x 10^{-9}	2.42 x 10^{-10}
2	Ratio of photocurrent to dark current	3.1 x 10^{1}	7.1 x 10^{2}
3	Quantum Efficiency (η)	73.93 %	75.35%
4	Specific Detectivity (D^*) $(mHz^{\frac{1}{2}}W^{-1})$	1.44 x 10^{9}	1.99 x 10^{9}
5	Responsivity (ℜ) (A/W)	17.9	18.21
6	NEP $(WHz^{-\frac{1}{2}})$	0.3 x 10^{-16}	0.21 x 10^{-16}

From the Table 4.2, we can observe that in comparison to the work reported in chapter 3 [134], the dark current is reduced significantly due to the presence of the heterojunction at the $n^0 - P^+$ interface. It acts as a barrier and prevents the diffusion of carriers from P^+ region to n^0 region. Thus, it is possible to obtain a reduced dark current. A very strong electric field created at the second hetero $(n^0 - P^+)$ interface in addition to the very strong electric field at the first hetero $(N^+ - n^0)$ interface sweeps away the photogenerated carriers very fast towards the electrodes, increasing carrier density being collected and hence there has been an enhancement in the specific detectivity, NEP, quantum efficiency and responsivity indicating the superior performance of the proposed double heterojunction in comparison to the single heterojunction photodetector at 30 µm [134].

4.6 Conclusion

A mercury cadmium telluride based double heterojunction, $N^{+} - CdTe/\, n^{0} - Hg_{0.824675}Cd_{0.175325}Te\, /P^{+} - Hg_{0.778299}Cd_{0.221701}Te$ n-i-p photodetector has been proposed to operate at a wavelength of 30 µm under a reverse bias of 0.5 V and at a cryogenic temperature of 77 K. The device has been simulated in the commercially available ATLAS™ TCAD tool. The results from ATLAS™ simulation are compared with the analytical modeling results and are found to be matching. It can be concluded that the double heterojunction photodetector designed showed substantial reduction in the dark current and superior performance in the optical characteristics like specific detectivity, noise equivalent power, quantum efficiency and responsivity in comparison to the single heterojunction photodetector operating at 30 µm wavelength.